Title

Improving the thermoelectric properties of half-Heusler TiNiSn through inclusion of a second full-Heusler phase: microwave preparation and spark plasma sintering of TiNi 1+x Sn

Permalink

Journal

ISSN

Authors

Birkel, Christina S
Douglas, Jason E
Lettiere, Bethany R
et al.

Publication Date

DOI

Copyright Information

Peer reviewed

Improving the thermoelectric properties of half-Heusler TiNiSn through inclusion of a second full-Heusler phase: Microwave preparation and Spark Plasma Sintering of TiNi$_{1+x}$Sn †

Christina S. Birkel,[ab] **Jason E. Douglas,**[bc] **Bethany R. Lettiere,**[b] **Gareth Seward,**[d] **Nisha Verma,**[c] **Yichi Zhang,**[a] **Tresa M. Pollock,**[bc] **Ram Seshadri,**[abc] **and Galen D. Stucky**[*ac]

Half-Heusler thermoelectrics offer the possibility to choose from a variety of non-toxic and earth-abundant elements. TiNiSn is of particular interest and – with its relatively high electrical conductivity and Seebeck coefficient – allows for optimization of its thermoelectric figure of merit, reaching values of up to 1 in heavily-doped and/or phase-segregated systems. In this contribution, we used an energy- and time-efficient process involving solid-state preparation in a commercial microwave oven and a fast consolidation technique, Spark Plasma Sintering, to prepare a series of Ni-rich TiNi$_{1+x}$Sn with small deviations from the half-Heusler composition. Spark Plasma Sintering plays an important role in the process by being a part of the synthesis of the material rather than solely a densification technique. Synchrotron powder X-ray diffraction and microprobe data confirm the presence of a secondary TiNi$_2$Sn full-Heusler phase within the half-Heusler matrix. We observe a clear correlation between the amount of full-Heusler phase and the lattice thermal conductivity of the samples, resulting in decreasing total thermal conductivity with increasing TiNi$_2$Sn fraction. This trend shows that phonons are scattered effectively as a result of the microstructure of the materials with full-Heusler inclusions in the size range of microns to tens of microns. The best performing samples with around 5% of TiNi$_2$Sn phase exhibit maximum figures of merit of almost 0.6 between 750 K and 800 K which is an increase of ca. 35% compared to the zT of the parent compound TiNiSn.

1 Introduction

Thermoelectric materials, which directly convert between thermal and electrical energy, could play a major role in the world's energy management. Their use in waste heat recovery, for example in automobiles, is an attractive and feasible goal for the near future.[1,2] Most efforts in thermoelectrics research deal with designing materials with increased conversion efficiency in order to allow for an economic use of the resulting thermoelectric systems. The greatest challenge lies in the inter-

dependency of the material properties manifested in the expression of the thermoelectric figure of merit, which is directly related to the conversion efficiency. The thermoelectric figure of merit is described as $zT = \alpha^2/(\rho \kappa) \times T$, where α is the Seebeck coefficient, T is the absolute temperature, ρ is the electrical resistivity and κ is the thermal conductivity.[3]

State-of-the-art bulk materials that currently offer the best possible balance between those different factors are Te-based systems (Bi$_2$Te$_3$,[4] PbTe,[4] LAST,[5] TAGS[6]), SiGe[7] and the Zintl compounds Yb$_{14}$Mn$_{1-x}$Al$_x$Sb$_{11}$[8] and Zn$_4$Sb$_3$.[9] Despite their high zT values of around 1 or even 1.5 in the case of LAST and TAGS, a major issue is the low earth crust abundance and high market price of at least one of their components. Amatya and Ram discuss these economic factors of different elements and particularly point out that the high price of Ge, Sb, Te and Yb containing materials may prohibit their use in any large-scale applications.[10]

Half-Heusler compounds, such as TiNiSn-based systems, are a promising class of thermoelectric materials with regard to elemental abundance since they con-

tain earth-abundant and non-toxic elements, such as Ti and Sn. Although they consist of three (or more) metals, they show semiconducting behavior which allows for reasonable electrical resistivities and relatively high Seebeck coefficients.[11,12] The drawback is their thermal conductivities, which are typically between $5\,\mathrm{Wm^{-1}K^{-1}}$ and $10\,\mathrm{Wm^{-1}K^{-1}}$, which are higher compared to those of current state-of-the-art materials.[4] Introducing segregated phases or nanostructures which scatter phonons efficiently has become one approach to lower the thermal conductivity without significantly influencing the electron transport within the system.[13–15] Recent reports show that the lattice thermal conductivity could be reduced drastically (around 50%) by introducing secondary (nanoscale) phases[16] and zT values as high as 0.9 in melt-spun (Hf,Zr)NiSn[17] and 1 in arc-melted (Ti,Zr,Hf)NiSn[18] can be reached, for example. It has to be noted that the decrease in thermal conductivity can be the result of various scattering mechanisms in these systems. They range from alloy scattering due to large differences in atomic mass of the present elements,[19] to point scattering on embedded nanoparticles[16,20,21] and grain boundary scattering promoted by nano- and microstructuring.[18] In order to demonstrate the relevance of all of these mechanisms, Biswas *et al.* combined them in a "panoscopic" approach to scatter heat-carrying phonons across integrated length scales which recently allowed them to fabricate a PbTe-SrTe compound with a reported zT of 2.2 at 915 K.[22]

Here, we investigate the possibility to increase zT of one of the most widely studied half-Heusler materials, TiNiSn. Annual production of the key elements due to high crustal abundance is very high, making it an attractive candidate for the large-scale use in thermoelectric devices. Instead of doping the material with heavier (Zr, Hf) or less-abundant and more expensive elements, such as Sb, we study the systematic addition of small amounts of Ni, creating a secondary full-Heusler $TiNi_2Sn$ phase within the half-Heusler matrix. Previously, our group has demonstrated that spontaneously formed $TiNi_2Sn$ within a TiNiSn matrix exhibits reduced thermal conductivity and enhanced zT.[23] However, in contrast to utilizing levitation melting, the $TiNi_{1+x}Sn$ compounds with $x = 0$, 0.02, 0.04, 0.06, 0.08, 0.1 and 0.15 were prepared by a time- and energy- efficient method involving first the solid state microwave reaction followed by consolidation through Spark Plasma Sintering. The samples are carefully characterized by means of synchrotron powder X-ray diffraction and electron microprobe analyses, in addition to measurement of thermoelectric properties.

2 Experimental

Inspired by recent reports on the microwave syntheses of intermetallic and oxide materials,[24,25] we have previously demonstrated the use of a commercial microwave to prepare half-Heusler compounds.[26] For the present study, we prepared 7 different $TiNi_{1+x}Sn$ samples with $x = 0$, 0.02, 0.04, 0.06, 0.08, 0.1 and 0.15. Briefly, the different metal powders (Ni (99.99%, Sigma Aldrich), Ti (99.7%, Sigma Aldrich), Sn (99.8%, Sigma Aldrich) were weighed out in a nitrogen-filled glovebox and loaded into silica tubes which were then removed from the glovebox and sealed under vacuum. Using granular carbon (Darco 12 mesh to 20 mesh, Sigma Aldrich) as an external susceptor material, the individual silica tubes were reacted in a commercial microwave oven at 100% power for 4 min. A more detailed description of this preparation method can be found in the previous publication.[26]

The products were then collected from the silica tube and first roughly crushed with a percussion mortar and then ball-milled with acetone in a WC container for 10 min using a SPEX 8000M Mixer/Mill. After drying in a crystallization dish, approximately 5 g of the fine powders were loaded into a high-density graphite die using graphite foil as a barrier between the powder and the die and consolidated into dense pellets using the Spark Plasma Sintering technique. A pressure of 50 MPa was applied before the temperature was raised to 1273 K with a heating rate of 50 K/min. The samples were pressed at that temperature for 10 min, followed by a 15 min cool down with decreasing pressure. The resulting cylindrical pellets were approximately 20 mm in diameter and 2 mm in thickness allowing all the different characterization techniques to be carried out on the same pellet. They were polished with SiC abrasive paper (different roughnesses) in order to remove the graphite.

Powder X-ray diffraction data were obtained on a Philips X'Pert with $CuK\alpha$ radiation. In addition, a small piece of the pellets was finely crushed and high resolution synchrotron powder diffraction data were collected at beamline 11-BM at the Advanced Photon Source (APS), Argonne National Laboratory using a wavelength of $\lambda = 0.440649\,\text{Å}$. Le Bail fits and Rietveld refinements were performed with TOPAS Academic V4.1.[27]

Electron Microprobe analyses were conducted using a Cameca SX100 equipped with 5 wavelength dispersive spectrometers (WDS). Probe Image and Probe for EPMA (Probe software Inc.) were used for acquisition of X-ray intensity maps and quantitative data respectively (see SI for analytical conditions). In order to visualize chemical compositional differences within the X-ray map data, individual element X-ray intensity channels were combined

into three channels of a color image to create a false color composite image of X-ray intensity for all elements.

For the TEM investigation, lamellae from specific locations of interest were made by focused ion beam (FIB, FEI DB235, Hillsboro, OR). Microstructure and microchemical characterization on the extracted lamellae was performed using a FEI Tecnai G2 Sphera TEM (FEI) equipped with energy dispersive X-ray spectroscopy. Dark-field imaging (DF) and bright field imaging (BF) along with point composition measurements were performed to identify the various phases present along with their orientation relation.

For measurement of the electronic properties bar-shaped pieces with the approximate dimensions $10\,\text{mm} \times 2\,\text{mm} \times 2\,\text{mm}$ were cut using a low-speed saw (Allied Inc.) with a diamond wafering blade. Seebeck coefficient and electrical resistivity in the temperature region between 300 K and 875 K were measured simultaneously on those samples using a ZEM-3 Ulvac instrument. The electronic transport properties were measured in two consecutive heating and cooling cycles. The data lie almost perfectly on top of each other but a slight decrease in power factor (lower resistivity and absolute Seebeck coefficient) could be observed for some of the samples.

For thermal diffusivity measurements disks, approximately 7.5 mm in diameter and 2 mm in thickness, were cut using wire electrical discharge machining (EDM, BROTHER HS-350) and sprayed with a layer of carbon paint in order to minimize errors in the emissivity. Thermal diffusivity was measured using the thermal flash technique between room temperature and 873 K under argon on an Anter Flashline 5000 system. The thermal conductivity was calculated using $\kappa = D d C_p$ where D is the thermal diffusivity, d is the density and C_p is the specific heat, respectively. The Cowan model for diffusivity and the Dulong-Petit molar heat capacity, $C_p = 3R$, were utilized. Densities were obtained on the same pieces using a pycnometer (Micromeritics AccuPyc 1330 Pycnometer) and were found to be $\geq$99% of the theoretical density. For microstructural investigations the remaining pieces were polished further in order to obtain a smooth surface for additional characterizations. Samples were fixed into an epoxy (Buehler Epomet) by hot compression mounting and polished using the following procedure: The samples were ground using silicon carbide abrasive paper and then polished to 0.25μm using colloidal diamond on cloth.

Field-emission scanning electron microscopy was performed on a FEI XL40 Sirion FEG microscope with an Oxford Inca X-ray system attached for chemical analysis. In addition, a FEI XL30 microscope equipped with a backscattered electron detector (BSE) was used to maximize the contrast between phases with similar atomic composition. After polishing the mounted samples (in epoxy), they were surrounded either with carbon tape or silver paste in order to prevent the sample from charging during imaging. Secondary electron microscopy images were collected with an acceleration voltage of 5 keV. Micrographs obtained in backscattering mode were collected with an accelerating voltage of 15 keV or 20 keV.

3 Results and discussion

3.1 Phase characterization

X-ray powder diffraction data of as-prepared and SPS treated samples are presented in Figure 1. Note that we collected high-resolution synchrotron XRD data for the consolidated compounds since all other characterization techniques were performed on those samples (Figure 1(b)). Both data sets include a zoom-in area on the right showing the strongest half-Heusler and full-Heusler peak, respectively.

The most intense peaks found in all of the XRD data of the as-prepared $\text{TiNi}_{1+x}\text{Sn}$ samples after microwave treatment match the strongest peaks corresponding to the half-Heusler phase (Figure 1(a)). All samples contain full-Heusler TiNi_2Sn as well as Ti_6Sn_5 and elemental Sn as additional phases. The intensity of the strongest full-Heusler peak seems to increase when comparing the sample with $x = 0$ to those with $x = 0.1$ and $x = 0.15$ which is to be expected due to the increasing amount of excess Ni.

The synchrotron XRD data of the consolidated materials show the presence of half-Heusler TiNiSn (main phase), full-Heusler TiNi_2Sn and metallic Sn, while the peaks of Ti_6Sn_5 can no longer be identified clearly. Furthermore, the intensity of the strongest full-Heusler compared to the strongest half-Heusler peak is much lower than what could be observed in the data of the as-prepared compounds. For example, samples with $x = 0$ and $x = 0.02$ only show very weak full-Heusler peaks which are hardly noticeable.

Figure 1(b) also includes an example of a two-phase Rietveld refinement for the sample with $x = 0.15$. The orange and the dark blue curves show the fits to the half-Heusler and full-Heusler phases, respectively. This sample was chosen because its XRD data exhibit the strongest full-Heusler peak among the studied compounds. Rietveld refinements of the synchrotron XRD data of all consolidated samples were performed (not shown here). The resulting cell parameters for the half-Heusler and the full-Heusler phases as well as the refined fraction of full-

Heusler present in the different compounds are shown in Figure 2.

Cell parameters of the half-Heusler phase are slightly larger than those reported in the literature[28,29] and increase with increasing x in TiNi$_{1+x}$Sn roughly following the Végard law. A similar trend was found by Hazama *et al.* who report improved thermoelectric properties as a result of interstitial Ni defects.[30] Cell parameters of the full-Heusler phase are slightly smaller than those reported in the literature.[31] No clear trend can be observed with varying composition which is probably due to the low intensity and broadness of the peaks.

Refined fractions of full-Heusler in the different samples are presented in Figure 2(c). The percentage of full-Heusler generally increases with increasing x composition as intended in this study. Here, it should be noted that the sample with $x = 0.04$ is an outlier and has a higher fraction of full-Heusler phase than samples with $x = 0.06$ and 0.08. Therefore, all thermoelectric data will be discussed as a funcion of full-Heusler fraction rather than as a function of the nominal composition x in TiNi$_{1+x}$Sn. Although this anomaly is unexpected, transport properties can be explained by the amount of full-Heusler phase in the different compounds.

3.2 Microstructural characterization

Figure 3(a+b) shows an example of the morphology of the compounds after the microwave preparation and after consolidation by SPS for the sample with $x = 0.06$. During the microwave preparation the metal powders melt and take the geometric form of the quartz tube. The specimens that are collected from the tube show large pores (hundreds of microns) without any predominant morphological features (Figure 3(a)). Additional images including different magnifications can be found in the Supplementary Information (Figure SI-1). After densification and polishing of the obtained pellets, the surface is very smooth with some small voids but no major cracks, proving the high density and good quality of the samples (Figure 3(b)). The image of the pellet's surface was obtained in backscattering mode which makes secondary phases visible through elemental contrast (see lighter areas in Figure 3(b)).

For a more detailed microstructural analysis, microprobe data were obtained on all of the samples. Here, only those for the best performing samples in terms of their figure of merit ($x = 0.02, 0.04, 0.06$) are presented (Figure 3(c)). The remaining images can be found in the Supplementary Information (Figure SI-2). Individual element X-ray intensity channels were combined into three channels of a color image to create a false color compos-

ite image of X-ray intensity for all elements. This allows the visualization of different phases and metal-rich areas. The majority phase of all samples is half-Heusler TiNiSn (dark green in Figures 3(c)) as is to be expected. The Ni-rich areas corresponding to the full-Heusler TiNi$_2$Sn phase are represented in a lighter green and can be found as smaller and larger inclusions (few microns to few tens of microns). Additional phases, such as binary Ni- and Ti-Sn phases and elemental Ti and Sn, can also be identified. Although the microprobe data represent random areas on the pellet's surfaces, an increasing amount of light green full-Heusler phase can be noted when comparing the TiNi$_{1+x}$Sn samples with increasing x. Notice again the large amount of full-Heusler in the (anomaly) sample with $x = 0.04$ which can be identified in the corresponding microprobe image (Figure SI-2).

An electron microscopy investigation was conducted for one of the samples with the highest figures of merit (Figure 4). A TEM lamella extracted from TiNi$_{1.06}$Sn was characterized to identify various phases present, their orientation relation and size scales. Energy dispersive X-ray spectroscopy (EDS) was used to identify the different phases and it revealed that the sample is a mixture of multiple phases consisting of half-Heusler TiNiSn, full-Heusler TiNi$_2$Sn, a binary phase Ni$_3$Sn$_4$ and unreacted Sn along with TiO$_2$. These findings complement the microprobe study which also showed the presence of multiple phases. The grain sizes for the various phases vary from nanometer sized in the case of the TiO$_2$ particles to a few microns for the full-Heusler and half-Heusler phases. The fH and hH phases do not share any orientation relationship (Figures 4) since the half-Heusler grain is not diffracting when the lamella is oriented according to the full-Heusler diffracting condition and *vice versa* (grains appear dark in the bright field image).

3.3 Electronic transport properties

The electrical resistivity and Seebeck coefficient for all of the different samples are presented in Figure 5 and room-temperature values are summarized in Table 1. Moreover, (near) room-temperature (and some maximum) values of all relevant transport data are plotted as a function of full-Heusler fraction in Figure 6. Resistivity and Seebeck coeffcient were obtained during two heating and cooling cycles and do not change significantly. Therefore, only the properties measured during the first heating segment are discussed here in order to avoid confusion in the plotted data.

All samples show semiconducting behavior, with a decreasing resistivity with increasing temperature. All Seebeck coefficients are relatively large and negative, indi-

Table 1 Fraction of fH phase, density (d), room-temperature resistivity (ρ), Seebeck coefficient (α), power factor (PF), figure of merit (zT) and maximum figure of merit of the different samples. Please note that the sample with $x = 0.04$ is an anomaly in this series since it contains a larger amount of the full-Heusler phase.

x in TiNi$_{1+x}$Sn	% of fH	d (gcm^{-3})	RT ρ (mΩcm)	RT α (μVK^{-1})	RT PF (mWm^{-1}K^{-2})	RT κ (Wm^{-1}K^{-1})	RT zT	max. zT
0	3.0	7.27	2.54	−129.4	0.66	5.14	0.04	0.37
0.02	4.2	7.26	4.46	−204.6	0.94	4.30	0.07	0.56
0.04	*7.9*	*7.14*	*1.6*	*−97.5*	*0.60*	*4.16*	*0.06*	*0.41*
0.06	6.2	7.32	3.27	−186.3	1.06	3.93	0.09	0.56
0.08	6.3	7.11	3.31	−193.4	1.13	4.34	0.09	0.54
0.1	9.3	7.34	1.36	−103.6	0.79	3.71	0.07	0.39
0.15	13.8	7.42	1.43	−104.7	0.77	3.61	0.07	0.38

cating that electrons are the majority carriers in these samples (*n*-type). The larger resistivities and absolute values of Seebeck coefficient agree well with the literature.[32,33] However, the exact numbers highly depend on the preparation and processing techniques and therefore the presence of additional phases as well as the microstructure of the studied materials.[34]

Particular attention needs to be paid to the sample with $x = 0.04$. Since it has a higher fraction of fH phase than samples with $x = 0.02$, 0.06 and 0.08 it does not follow the same trend. However, all electronic properties can be understood when discussed with the right amount of full-Heusler which still makes it a good example of the overall consistency. Samples with fH fraction above 6% ($x = 0.04$, 0.1, 0.15) clearly show a "more metallic" behavior. The resistivity curves are flatter and one can even observe a small increase in resistivity at high temperatures for samples with $x = 0.1$ and 0.15. Similar characteristics can be found in the Seebeck coefficients. All samples, except for $x = 0.1$ and 0.15, first show an increase in absolute Seebeck coefficient before it decreases again. This is a typical behavior for semiconducting compounds where electron-hole pairs are excited across the energy gap and the opposite contribution to the Seebeck coefficient reduces the absolute Seebeck coefficient. This trend cannot be observed for samples with the highest excess in Ni, $x = 0.1$ and 0.15, where we find a significant decrease in absolute Seebeck coefficient. The same effect is revealed in the electronic contribution of the thermal conductivity as an increase in κ_{el} for samples with x larger than 6% which will be discussed in more detail in section 3.4.

To further compare the various samples, room-temperature values are plotted as a function of full-Heusler fraction (Figure 6). Room-temperature resistivities and absolute Seebeck coefficients first increase with increasing fH fraction and then decrease again indicating lower carrier concentrations for $x = 0.02$, 0.06, 0.08 and

higher ones for $x = 0.04$, 0.1, 0.15 (Figure 6 (a+b)). This results in a similar trend in the room-temperature power factors (Figure 6 (c)). Overall, samples with fH fractions of around 5% ($x = 0.02$, 0.06, 0.08) show the highest power factors (highlighted inside the orange circle in Figure 6 (c+d)) with room-temperature power factor (PF) of around $1\,\text{mWm}^{-1}\text{K}^{-2}$.

3.4 Thermal transport properties

The results of the analysis of the thermal conductivity measurements are presented in Figure 7 and (near) room-temperature values are plotted as a function of full-Heusler fraction in Figure 6 (e-h). Thermal conductivity was calculated from the thermal diffusivity D, the density of the samples d and the Dulong-Petit heat capacity C_p using $\kappa = DdC_p$. Thermal diffusivities were measured during one heating and one cooling cycle and the curves lie almost perfectly on top of each other. Here, only the resulting data obtained during the heating segment are presented to enhance data clarity. Room-temperature values were neglected since they were not physically meaningful.

Thermal conductivity of the initial TiNiSn sample is found to be between $5\,\text{Wm}^{-1}\text{K}^{-1}$ and $6\,\text{Wm}^{-1}\text{K}^{-1}$ which is comparable to numbers reported in the literature.[35,36] The total thermal conductivity is the sum of electronic, lattice and bipolar contributions and TiNiSn shows a bipolar behavior, which is visible as a decreasing κ followed by an increase above a certain temperature. This can be attributed to excited carriers at high temperatures due to the small bandgap of TiNiSn.

Lorenz numbers were determined from experimental Seebeck coefficients using an SPB model[37,38] (see Figure 7(b)) in order to calculate the electronic contribution to the thermal conductivity with $\kappa_{el} = LT/\rho$, where L is the Lorenz number, T is the temperature and ρ the electrical resistivity. All Lorenz numbers are significantly lower

than the value for the free electron model ($2.44\,W\Omega K^{-2}$) and are comparable to previously published numbers.[26] Within the $TiNi_{1+x}Sn$ series, the samples with the highest PF ($x = 0.02, 0.06, 0.08$) show the lowest Lorenz numbers ($1.6\,W\Omega K^{-2}$) around room temperature) whereas the samples with higher fractions of full-Heusler phase exhibit higher values ($1.85\,W\Omega K^{-2}$).

The major contribution to the thermal conductivity is the lattice thermal conductivity (see Figure 7(c+d)) which also agrees well with previously published results.[26] Naturally, the electronic contribution to the thermal conductivity mirrors the calculated Lorenz numbers where the samples with the highest fraction of full-Heusler phase ($x = 0.1, 0.15$) exhibit the highest κ_{el}. Values increase with increasing temperature which is in accordance with decreasing resistivity in semiconducting samples. The reason why the initial sample with $x = 0$ shows a slightly higher κ_{el} may be that this sample contains a higher amount (about 8 mol%) of metallic Sn than the other samples (2-4 mol%) (see Figures 1(b) and SI-2).

However, the lattice thermal conductivity does not seem to be affected by the Sn segregations since the compound with $x = 0$ has the largest amount of Sn but also the highest κ-κ_{el} among all the samples studied here (Figure 7(d)). When introducing full-Heusler $TiNi_2Sn$ as a secondary phase, κ-κ_{el} drops significantly. It decreases continuously with increasing amount of fH phase, first getting reduced by about $1\,Wm^{-1}K^{-1}$ in the case of the smaller x fractions and then by about $2\,Wm^{-1}K^{-1}$ in the case of the higher x fractions ($x = 0.1, 0.15$). This shows that there is a correlation between amount of full-Heusler phase and decrease in thermal conductivity mainly unaffected by the presence of other metal-rich phases.

This occurrence is reflected in the overall thermal conductivity of the samples. Room-temperature values also decrease monotonically with increasing amount of full-Heusler phase due to the predominant behavior of the lattice contribution (see Figure 6 (e+h)). Therefore, the compounds with $x = 0.1$ and 0.15 exhibit the lowest room-temperature thermal conductivities (3.6-$3.7\,Wm^{-1}K^{-1}$) which is a reduction of about 30% compared to the initial TiNiSn sample. At higher temperatures on the other hand, they show higher thermal conductivities than the rest of the half-Heusler/full-Heusler compounds ($x = 0.02, 0.04, 0.06, 0.08$) due to the larger electronic contribution.

3.5 Thermoelectric figure of merit

The figures of merit were calculated from the appropriate fits of the electrical conductivity, Seebeck coefficient and thermal conductivity and are presented in Figure 8.

Room-temperature zT values of all full-Heusler/half-Heusler compounds are higher (by almost a factor of two) compared to the initial TiNiSn sample which can mainly be attributed to the reduced thermal conductivity in those compounds (see Figure 6 (i)). The three samples with the highest room-temperature zT of almost 0.1 are the samples with fractions of full-Heusler phase of around 5% ($x = 0.02, 0.06, 0.08$, see orange circle in Figure 6 (i)). These are also the best performing samples with the highest maximum figure of merit of almost 0.6 at around 800 K (Figure 6 (j)) which is an increase of ca. 35% compared to the initial half-Heusler material ($zT = 0.35$). The other samples show maximum figures of merit which are comparable or only slightly larger than the one of the sample with $x = 0$. Although those samples also show a reduced thermal conductivity, the reason for that is the combination of lower power factors (more "metallic" samples) and the larger thermal conductivities at high temperatures due to the stronger electronic contribution. In those samples, the effect of phonon scattering which reduces the lattice thermal conductivity does not outdo the negative effect of the "more metallic" nature of the compounds due to the inclusion of the full-Heusler phase.

4 Conclusion

We have presented a fairly straightforward way to increase the figure of merit of the promising thermoelectric material TiNiSn through inclusion of the secondary $TiNi_2Sn$ full-Heusler phase. In contrast to other approaches involving doping with heavier elements for example, only a small amount of excess of Ni was introduced in these compounds. The materials were prepared in an energy- and time-efficient way using a commercial microwave oven and a Spark Plasma Sintering apparatus. It has to be noted that the Spark Plasma Sintering step not only consolidates the materials but also plays an active role in the preparation by reducing the amount of additional phases. X-ray diffraction data and microprobe investigations show the presence of an increasing amount of full-Heusler phase within the half-Heusler matrix which can be correlated to the transport properties of the different samples. The total thermal conductivity clearly decreases with increasing x in $TiNi_{1+x}Sn$ which is a result of the reduced lattice thermal conductivity in the samples with larger amounts of micron-sized full-Heusler inclusions. This result shows that phonons are effectively scattered as a result of the irregular microstructure of the studied samples. The increase in figure of merit of about

35% is quite remarkable considering that only a small amount of excess Ni was introduced to form the *in-situ* secondary phase. We believe that further increase in figure of merit is possible by additional doping with heavier elements which might increase the Seebeck coefficient and lower the thermal conductivity even further due to alloy scattering of short-wavelength phonons.

5   Acknowledgement

References

1   J. Bass, N. Elsner, S. Ghamaty, V. Jovanovic and D. Krommenhoek, Diesel Engine-Efficiency and Emissions Research Conference, Chicago, Illinois, 2005.

2   J. LaGrandeur, IEEE 25th International Conference on Thermoelectrics, Vienna, Austria, 2006.

3   G. J. Snyder and E. S. Toberer, *Nat. Mater.*, 2008, **7**, 105–114.

4   D. Rowe, *CRC Handbook of Thermoelectrics*, Boca Raton, 1995.

5   K. F. Hsu, S. Loo, F. Guo, W. Chen, J. S. Dyck, C. Uher, T. Hogan, E. Polychroniadis and M. G. Kanatzidis, *Science*, 2004, **303**, 818–821.

6   S. H. Yang, T. J. Zhu, T. Sun, J. He, S. N. Zhang and X. B. Zhao, *Nanotechnology*, 2008, **19**, 245707.

7   H. R. Meddins and J. E. Parrott, *J. Phys. C: Solid State Phys.*, 1976, **9**, 1263–1276.

8   S. R. Brown, S. M. Kauzlarich, F. Gascoin and G. J. Snyder, *Chem.Mater.*, 2006, **18**, 1873–1877.

9   T. Caillat, J.-P. Fleurial and A. Borshchevsky, *J. Phys. Chem. Solids*, 1997, **58**, 1119–1125.

10   R. Amatya and R. J. Ram, *J. Electron. Mater.*, 2012, **41**, 1011–1019.

11   J. Pierre, R. V. Skolozdra, J. Tobola, S. Kaprzyk, C. Hordequin, M. A. Kouacou, I. Karla, R. Currat and E. Leliévre-Berna, *J. Alloys Compd.*, 1997, **262-263**, 101–107.

12   J. Tobola and J. Pierre, *J. Alloys Compd.*, 2000, **296**, 243–252.

13   S. J. Poon, D. Wu, S. Zhu, W. Xie, T. Tritt, P. Thomas and R. Venkatasubramanian, *J. Mater. Res.*, 2011, **26**, 2795–2802.

14   N. J. Takas, P. Sahoo, D. Misra, H. Zhao, N. L. Henderson, K. Stokes and P. F. P. Poudeu, *J. Electron. Mater.*, 2011, **40**, 662–669.

15   J. P. A. Makongo, D. K. Misra, X. Zhou, A. Pant, M. R. Shabetai, X. Su, C. Uher, K. L. Stokes and P. F. P. Poudeu, *JACS*, 2011, **133**, 18843–52.

16   J. P. A. Makongo, D. K. Misra, J. R. Salvador, N. J. Takas, G. Wang, M. R. Shabetai, A. Pant, P. Paudel, C. Uher, K. L. Stokes and P. F. P. Poudeu, *J. Solid State Chem.*, 2011, **184**, 2948–2960.

17   C. U. I. Yu, T.-j. Zhu, K. A. I. Xiao, J.-j. Shen, S.-h. Yang and X.-b. Zhao, *J. Electron. Mater.*, 2010, **39**, 2008–2012.

18   S. Populoh, M. H. Aguirre, O. C. Brunko, K. Galazka, Y. Lu and A. Weidenkaff, *Scripta Materialia*, 2012, **66**, 1073–1076.

19   X. Yan, W. Liu, H. Wang, S. Chen, J. Shiomi, K. Esfarjani, H. Wang, D. Wang, G. Chen and Z. Ren, *Energy Environ. Sci.*, 2012, **5**, 7543–7548.

20   H.-H. Xie, C. Yu, T.-J. Zhu, C.-G. Fu, G. J. Snyder and X.-B. Zhao, *Appl. Phys. Lett.*, 2012, **100**, 254104.

21   Y. W. Chai and Y. Kimura, *Appl. Phys. Lett.*, 2012, **100**, 033114.

22   K. Biswas, J. He, I. D. Blum, C.-I. Wu, T. P. Hogan, D. N. Seidman, V. P. Dravid and M. G. Kanatzidis, *Nature*, 2012, **489**, 414–418.

23   J. E. Douglas, C. S. Birkel, M.-S. Miao, C. J. Torbet, G. D. Stucky, T. M. Pollock and R. Seshadri, *Appl. Phys. Lett.*, 2012, **101**, 183902.

24   K. Biswas, S. Muir and M. A. Subramanian, *Mater. Res. Bull.*, 2011, **46**, 2288–2290.

25   A. Birkel, K. A. Denault, N. C. George, C. E. Doll, B. Hery, A. A. Mikhailovsky, C. S. Birkel, B.-C. Hong and R. Seshadri, *Chem. Mater.*, 2012, **24**, 1198–1204.

26   C. S. Birkel, W. G. Zeier, J. E. Douglas, B. R. Lettiere, C. E. Mills, G. Seward, A. Birkel, M. L. Snedaker, Y. Zhang, G. J. Snyder, T. M. Pollock, R. Seshadri and G. D. Stucky, *Chem. Mater.*, 2012, **24**, 2558–2565.

27   A. A. Coelho, *Topas Academic V4.1*, Software, Coelho Software, Brisbane (Australia), 2007.

28   W. Jeitschko, *Metall. Trans.*, 1970, **1**, 3159–3162.

29   C. B. H. Evers, C. G. Richter, K. Hartjes and W. Jeitschko, *J. Alloys Compd.*, 1997, **252**, 93–97.

30   H. Hazama, M. Matsubara, R. Asahi and T. Takeuchi, *J. Appl. Phys.*, 2011, **110**, 063710.

31   J. Pierre, R. V. Skolozdra, Y. K. Gorelenko and M. Kouacou, *J. Magn. Magn. Mater.*, 1994, **134**, 95–105.

32   S. Bhattacharya, A. L. Pope, R. T. Littleton IV, T. M. Tritt, V. Ponnambalam, Y. Xia and S. J. Poon, *Appl. Phys. Lett.*, 2000, **77**, 2476–2478.

33   S. Bhattacharya, M. Skove, M. Russell, T. M. Tritt, Y. Xia, V. Ponnambalam, S. Poon and N. Thadhani, *Phys. Rev. B*, 2008, **77**, 184203.

34   Y. Gelbstein, N. Tal, A. Yarmek, Y. Rosenberg, M. P. Dariel, S. Ouardi, B. Balke, C. Felser and M. Koehne, *J. Mater. Res.*, 2011, **26**, 1919–1924.

35   S.-W. Kim, Y. Kimura and Y. Mishima, *Intermetallics*, 2007, **15**, 349–356.

36   H. Muta, T. Kanemitsu, K. Kurosaki and S. Yamanaka, *J. Alloys Compd.*, 2009, **469**, 50–55.

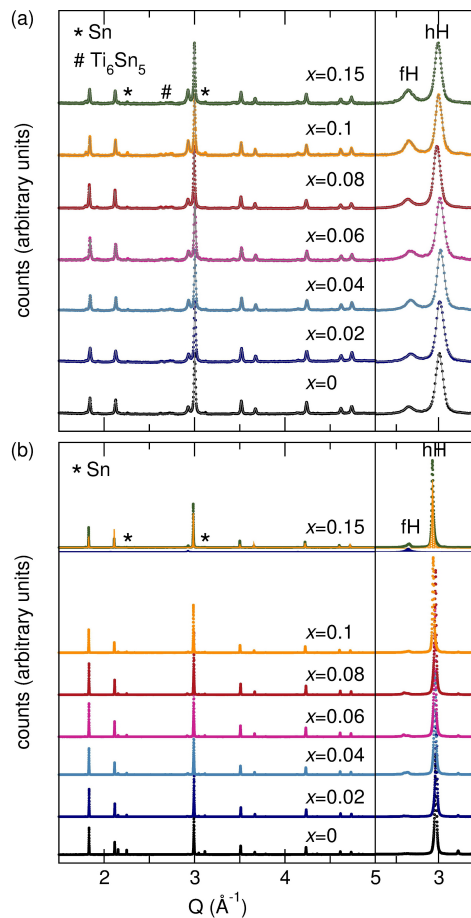37   A. F. May, E. S. Toberer, A. Saramat and G. J. Snyder, *Phys Rev. B*, 2009, **80**, 125205.

38 A. F. May and G. J. Snyder, in *Thermoelectrics Handbook: Thermo-electrics and its Energy Harvesting*, 2012, ch. 11.

Fig. 1 (a) X-ray powder diffraction data (filled dots) and le Bail fits of full-Heusler and half-Heusler crystal structure (solid lines) of as-prepared $TiNi_{1+x}Sn$ samples, * and # indicating Sn and Ti_6Sn_5 impurity phases, respectively, (b) Synchrotron X-ray powder diffraction data of $TiNi_{1+x}Sn$ samples after SPS consolidation, * indicating Sn impurity phase. As an example of Rietveld refinement, fits of the half-Heusler and the full-Heusler phases are presented for the sample with $x = 0.15$. $Q = 2\pi/d$ represents the momentum transfer function; $Q = 4\pi\sin(\theta/\lambda)$.
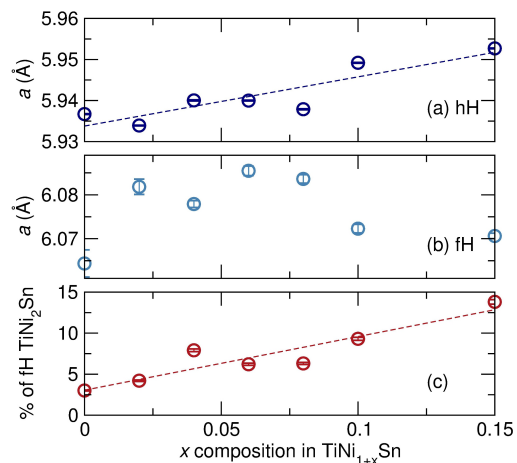
Fig. 2 Cell parameters of the half-Heusler phase (a), full-Heusler phase (b) and percentage of full-Heusler phase (c) in the different compounds calculated from Rietveld refinements. Lines are meant to guide the eye.
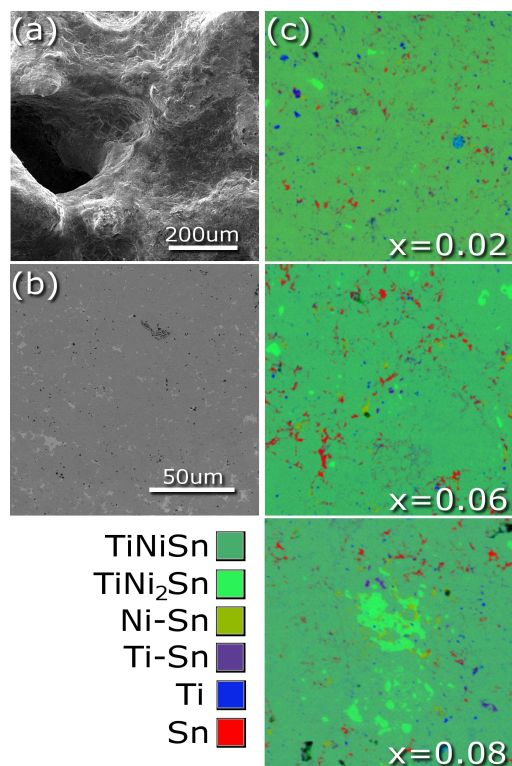

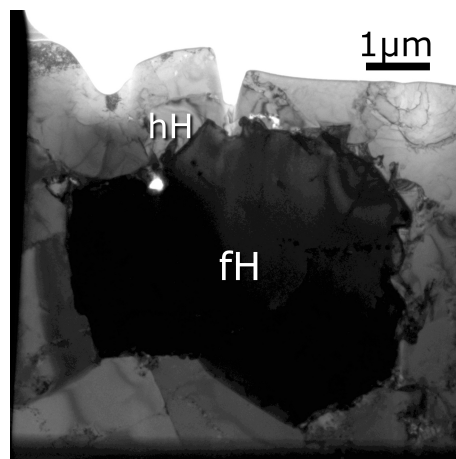**Fig. 4** TEM investigation of $TiNi_{1.06}Sn$: Bright field image where the fH grain is diffracting and the hH grain is not, showing that the phases do not share an orientation relationship.
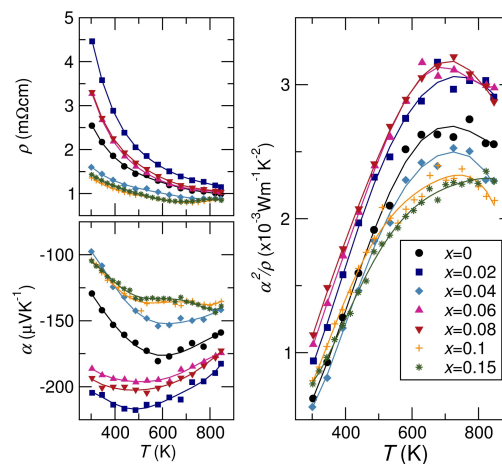

Fig. 3 SEM images of as-prepared (a) and consolidated (b) $TiNi_{1.06}Sn$. Note that (a) and (b) were obtained in secondary electron and backscattering mode, respectively. (c) Microprobe analysis of the best performing samples ($x = 0.02, 0.06, 0.08$) showing the different phases and metal-rich areas. Images are $128\mu m \times 128\mu m$.

Fig. 5 Electronic properties (resistivity, Seebeck coefficient and power factor) of the different $TiNi_{1+x}Sn$ samples. Filled symbols and solid lines represent data and fits, respectively.

Fig. 7 Total thermal conductivity (a), Lorenz number (b), electronic and lattice contribution of thermal conductivity (c+d) of the different TiNi$_{1+x}$Sn samples.
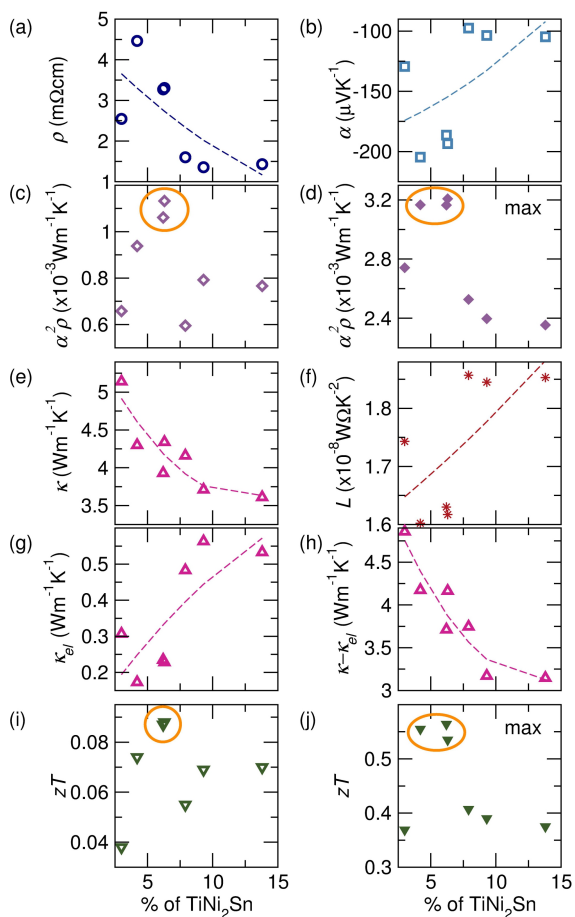

Fig. 6 (a) RT resistivity, (b) RT Seebeck coefficient, (c) RT power factor, (d) maximum power factor, (e) (near) RT total thermal conductivity, (f) Lorenz number, (g) (near) RT electronic thermal conductivity, (h) (near) RT lattice thermal conductivity, (i) RT figure of merit and (j) maximum figure of merit as a function of full-Heusler fraction. The circles highlight the best performing samples. Lines are meant to guide the eye.
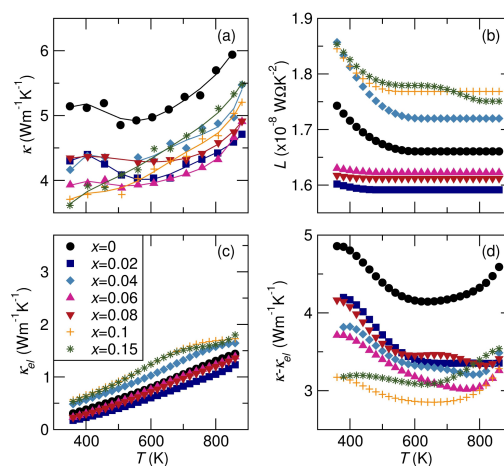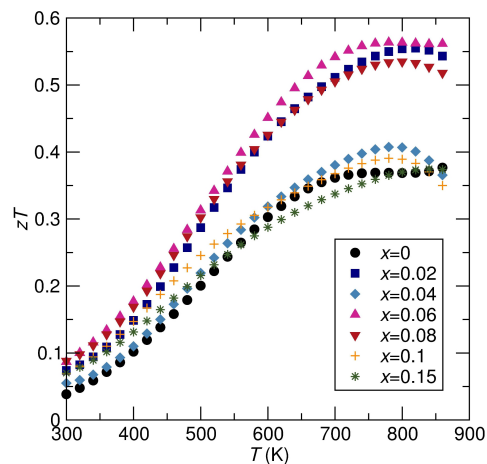

Fig. 8 Thermoelectric figure of merit of the different TiNi$_{1+x}$Sn samples.